

Rare Occasions: Tidal Disruption Events Rarely Power the AGNs Observed in Dwarf Galaxies

JOANNE TAN,^{1,2,3} GUANG YANG (杨光),^{4,5,6,7,2,3} JONELLE L. WALSH,^{2,3} W. N. BRANDT,^{8,9,10} BIN LUO,¹¹
FRANZ E. BAUER,^{12,13,14} CHIEN-TING CHEN,¹⁵ MOUYUAN SUN,¹⁶ AND YONGQUAN XUE^{17,18}

¹Max-Planck-Institut für Astrophysik, Karl-Schwarzschild-Straße 1, D-85748, Garching, Germany

²Department of Physics and Astronomy, Texas A&M University, College Station, TX, 77843-4242 USA

³George P. and Cynthia Woods Mitchell Institute for Fundamental Physics and Astronomy, Texas A&M University, College Station, TX, 77843-4242 USA

⁴Nanjing Institute of Astronomical Optics & Technology, Chinese Academy of Sciences, Nanjing 210042, China

⁵CAS Key Laboratory of Astronomical Optics & Technology, Nanjing Institute of Astronomical Optics & Technology, Nanjing 210042, China

⁶Kapteyn Astronomical Institute, University of Groningen, P.O. Box 800, 9700 AV Groningen, The Netherlands

⁷SRON Netherlands Institute for Space Research, Postbus 800, 9700 AV Groningen, The Netherlands

⁸Department of Astronomy and Astrophysics, 525 Davey Lab, The Pennsylvania State University, University Park, PA 16802, USA

⁹Institute for Gravitation and the Cosmos, The Pennsylvania State University, University Park, PA 16802, USA

¹⁰Department of Physics, 104 Davey Laboratory, The Pennsylvania State University, University Park, PA 16802, USA

¹¹School of Astronomy and Space Science, Nanjing University, Nanjing, Jiangsu 210046, China

¹²Instituto de Astrofísica, Facultad de Física, Pontificia Universidad Católica de Chile, Casilla 306, Santiago 22, Chile

¹³Millennium Institute of Astrophysics, Nuncio Monseñor Sótero Sanz 100, Providencia, Santiago, Chile

¹⁴Space Science Institute, 4750 Walnut Street, Suite 205, Boulder, Colorado 80301

¹⁵Astrophysics Office, NASA Marshall Space Flight Center, ZP12, Huntsville, AL 35812, USA

¹⁶Department of Astronomy, Xiamen University, Xiamen, Fujian 361005, People's Republic of China

¹⁷CAS Key Laboratory for Research in Galaxies and Cosmology, Department of Astronomy, University of Science and Technology of China, Hefei 230026, China

¹⁸School of Astronomy and Space Sciences, University of Science and Technology of China, Hefei 230026, China

ABSTRACT

Tidal disruption events (TDEs) could be an important growth channel for massive black holes in dwarf galaxies. Theoretical work suggests that the observed active galactic nuclei (AGNs) in dwarf galaxies are predominantly TDE-powered. To assess this claim, we perform variability analyses on the dwarf-hosted AGNs detected in the 7 Ms *Chandra* Deep Field-South (CDF-S) survey, with observations spanning ≈ 16 years. Based on the spectral energy distribution (SED) modeling with X-CIGALE, we select AGNs hosted by dwarf galaxies (stellar mass below $10^{10} M_{\odot}$). We focus on X-ray sources with full-band detections, leading to a sample of 78 AGNs ($0.122 \leq z \leq 3.515$). We fit the X-ray light curves with a canonical TDE model of $t^{-5/3}$ and a constant model. If the former outperforms the latter in fitting quality for a source, we consider the source as a potential TDE. We identify five potential TDEs, constituting a small fraction of our sample. Using true- and false-positive rates obtained from fitting models to simulated light curves, we perform Bayesian analysis to obtain the posterior of the TDE fraction for our sample. The posterior peaks close to zero (2.56%), and we obtain a $2\text{-}\sigma$ upper limit of 9.80%. Therefore, our result indicates that the observed AGNs in dwarf galaxies are *not* predominantly powered by TDEs.

1. INTRODUCTION

Massive black holes (BHs) are common in galactic centers (e.g., Kormendy & Ho 2013). Stars approaching the BH can be pulled apart by the BH's tidal force, when

the tidal force has surpassed the star's self-gravity (e.g., Rees 1988). While some of the stellar materials get expelled at high velocities, the remainder can get accreted, feeding the BH at super-Eddington rates and causing a bright flare that lasts for several years. Such events are known as tidal disruption events (TDEs).

The contribution of TDEs to overall BH growth might depend on the BH mass (M_{BH}). The dynamical models of Magorrian & Tremaine (1999) estimated that TDEs

can account for $\sim 10^6 M_\odot$ BH growth across cosmic history, independent of galaxy luminosity. This amount of BH growth is negligible for massive BHs, whose dominant growth channel should be cold-gas accretion. However, for low-mass BHs ($M_{\text{BH}} \lesssim 10^7 M_\odot$), the TDE-related BH growth can account for a large fraction of the total M_{BH} (see also, e.g., Wang & Merritt 2004; Stone & Metzger 2016; Greene et al. 2020 for similar conclusions). Therefore, TDEs could be a crucial ingredient for the growth of the low-mass BHs hosted by dwarf galaxies (stellar mass, $M_* \lesssim 10^{10} M_\odot$).

Zubovas (2019) modeled the active galactic nucleus (AGN) duty cycle powered by TDEs in dwarf galaxies, and found the predicted TDE-powered AGN fraction ($\gtrsim 0.5\%$) is consistent with the observed AGN fraction, with the assumption that the occupation fraction in dwarf galaxies is close to unity. Their result suggests that the observed AGNs in dwarf galaxies could be predominantly driven by TDEs. This theoretical conclusion is testable from observations: one can investigate the temporal behavior of AGNs detected in dwarf galaxies and determine if they are powered by TDEs. We perform such a study in this work.

The TDE flares mainly emit at UV and X-ray wavelengths (e.g., Rees 1988). Compared to UV photons, X-rays are less affected by obscuration due to their high penetrating power. Therefore, X-ray observations are ideal for the search for TDEs. Indeed, X-ray facilities have successfully identified many TDE candidates. For example, 2XMM J184725.1-631724 is an ultrasoft X-ray flare discovered by *XMM-Newton* (Lin et al. 2011). The intensive multiwavelength follow-up observations strongly support the flare being a TDE (Lin et al. 2018). RBS 1032 is a decaying X-ray source detected by the multi-epoch data of *ROSAT* (Fischer et al. 1998). It also has a supersoft spectrum in all *ROSAT* epochs (Ghosh et al. 2006). The *XMM-Newton* follow-up observations confirm that its light curve follows the $t^{-5/3}$ evolution track, a fundamental TDE signature (Maksym et al. 2014). From optical observations, the host galaxy of RBS 1032 is a dwarf galaxy at $z = 0.024$ (Ghosh et al. 2006). More recently, the eROSITA telescope (Predehl et al. 2021) onboard the SRG observatory (Sunyaev et al. 2021) has discovered a sample of 13 TDEs (Sazonov et al. 2021), which are confirmed by follow-up optical observations.

Given the advantages and successes of X-ray TDE searches, we choose to utilize the 7 Ms *Chandra* Deep Field-South (CDF-S) data (Luo et al. 2017, L17 hereafter) to examine if the AGNs in dwarf galaxies are powered by TDEs, as hypothesized by Zubovas (2019). The 7 Ms CDF-S is currently the deepest X-ray sur-

vey (see Xue 2017 for a review), enabling the detection of faint AGNs in dwarf galaxies. The CDF-S observations span a temporal baseline of ≈ 16 years. This long baseline significantly benefits our TDE search, because TDE light curves have stronger flux changes toward longer timescales. Short-term (\lesssim a few months) variability analyses may not be able to effectively differentiate TDEs from the variability of ordinary AGNs (e.g., Maksym et al. 2014; Yang et al. 2016). Another advantage of the long baseline is the increased probability of a TDE occurrence. The CDF-S is also accompanied by deep observations from UV to radio wavelengths (e.g., Elbaz et al. 2011; Guo et al. 2013). The multiwavelength data are critical for reliably estimating M_* and thereby selecting for dwarf galaxies for our study.

This paper is structured as follows. In Section 2, we describe the observations, source selection, and spectral energy distribution (SED) fitting of the sources. In Section 3, we perform variability analyses and identify TDE candidates. Next, we constrain the TDE fraction in Section 4. In Section 5, we compare the ratio of fluxes between pairs of epochs for each source and examine the distribution of the effective power-law photon index, Γ . These diagnostics serve to identify the model-independent changes in fluxes and to determine whether the sources have Γ values typical of TDEs, respectively. Lastly, we summarize our results and discuss future prospects in Section 6.

Throughout this paper, we assume a cosmology with $H_0 = 70 \text{ km s}^{-1} \text{ Mpc}^{-1}$, $\Omega_M = 0.3$, and $\Omega_\Lambda = 0.7$. We use AB magnitudes and quote uncertainties at the $1-\sigma$ (68%) confidence level, unless stated otherwise. We define ‘‘AGNs’’ to include both ordinary AGNs and TDE-powered AGNs; we emphasize that ‘‘ordinary AGNs’’ refer only to AGNs powered by typical gas accretion.

2. DATA AND SOURCE SELECTION

2.1. Observations

This work, based on the 7 Ms CDF-S X-ray data, employs a list of *Chandra* datasets, obtained by the *Chandra* X-ray Observatory, contained in the *Chandra* Data Collection (CDC) 270 doi:10.25574/cdc.270. There are a total of 102 observations, which were taken from October 1999 to March 2016. The median exposure time of the 102 observations is ≈ 56 ks. All of the 102 CDF-S observations utilized the *Chandra* Advanced CCD Imaging Spectrometer imaging array (ACIS-I, Garmire et al. 2003). More details about the observations can be found in Section 2.1 of L17. We use the ACIS EXTRACT (Broos et al. 2010) data products from L17 (see Section 2.2 of L17 for details on data reduction).

Most CDF-S sources have low signal-to-noise (S/N) in single observations. Thus, to improve the S/N of the sources, we bin data from observations made around similar times to form several “epochs”. From the 102 observations, we compile five epochs for each source, and each of these epochs consists of observations that sum up to ~ 1 –2 Ms of exposure time. Similar to Yang et al. (2016), the bins are chosen such that as much data as possible are included in the shortest span of time possible. This is to minimize the variability effects within each epoch. The epochs’ details are listed in Table 1.

Table 1. Epochs formed from 102 observations

Epoch	Start date	End date	W_{bin} (yr) ^a	T_{exp} (Ms) ^b	N_{obs} ^c
1	1999 Oct	2000 Dec	1.19	0.931	11
2	2007 Sep	2007 Nov	0.12	0.960	12
3	2010 Mar	2010 Jul	0.35	1.956	31
4	2014 Jun	2015 Jan	0.57	1.854	31
5	2015 Mar	2016 Mar	1.02	1.027	17

NOTE—

^a Bin width, i.e., the time span between the start and end dates.

^b Total exposure time of all observations in an epoch.

^c Number of observations in each epoch.

2.2. Source selection

We first select our sources from the main catalog of the 7 Ms CDF-S survey (hereafter the L17 catalog). From these, we narrow down to sources with a counterpart in the CANDELS multi-wavelength catalog in the GOODS-South Field (Guo et al. 2013, hereafter the CANDELS catalog), adopting the counterpart-matching results from the L17 catalog. We find a subset of 674 sources that are in both catalogs, covering a sky region of ≈ 170 arcmin².

Next, we remove all sources that are classified as “Galactic star” (identified spectroscopically) in the L17 catalog and retain only sources that are classified as “AGN” or “Galaxy”. At this stage, we have 670 sources. We then also remove two sources that are confirmed X-ray transients, i.e. CDF-S XT1 (Bauer et al. 2017) and CDF-S XT2 (Xue et al. 2019), as these sources are unlikely to have AGNs and we are focusing only on galaxies that host AGNs to search for potential TDEs.

From the 668 sources, we filter for sources with full-band (0.5–7.0 keV) detections. We use full-band photometry to construct light curves and search for TDE signatures as it encompasses both the soft and hard bands, making it the widest available band and yield-

ing the largest number of counts for each source. This gives us 591 sources. Lastly, to select low-mass sources, we perform multi-wavelength SED fitting for these 591 sources using X-CIGALE (Boquien et al. 2019; Yang et al. 2020; see Section 2.3 for details). We define low-mass sources to be those with $M_* \leq 10^{10} M_{\odot}$, as determined by X-CIGALE. This criterion gives us 144 low-mass sources. In this work, we are focusing on AGNs hosted by dwarf galaxies; thus, we select for low-mass sources that L17 have classified as “AGN”. Ultimately, we obtain 78 X-ray detected AGNs in low-mass galaxies with redshift (z , from L17) between 0.122 and 3.515. The properties of our sample are tabulated in Table 2.

2.3. SED fitting with X-CIGALE

In order to measure M_* , we utilize X-CIGALE¹ (Boquien et al. 2019; Yang et al. 2020), an SED-modelling tool with the capability to build AGN and galaxy SEDs in the X-ray to IR wavelength range. We obtain the bandpass fluxes of 17 filters from the UV to mid-IR wavelengths from the CANDELS catalog; more details about the filters and data used can be found in Guo et al. 2013 (G13 hereafter). We also use X-ray fluxes from L17 in the hard band (2–7 keV) or in the full band. We prioritize fluxes in the hard band, as it is the least obscured among the three available bands and X-CIGALE requires using unobscured data for the SED fitting. For sources that are not detected in the hard band, we use their full-band fluxes instead. We use the hard-band detected fluxes for 358 sources (60.6%) and full-band detected fluxes for the remaining 233 sources (39.4%).

The X-CIGALE modules we use are listed in Table 3, along with their respective fitting parameters. X-CIGALE requires the assumption of a parametric star formation history (SFH) in order to model the SED of a galaxy. We adopt the delayed- τ SFH model. The stellar spectrum is computed from the SFH and the Bruzual & Charlot (2003) single stellar population (SSP) models, assuming a Chabrier (2003) initial mass function (IMF) and a metallicity of $Z = 0.02$ (solar). For the computation of nebular emission, we adopt the NEBULAR module, which considers both continuum and line nebular emission.

To compute galactic dust attenuation, we adopt DUSTATT_MODIFIED_STARBURST, a module based on the Calzetti et al. (2000) starburst attenuation, and extended with the Leitherer et al. (2002) curve between the Lyman break and 150 nm. We fix the color excess ratio between the old and young stellar populations to unity, and vary the color excess of starlight for both the

¹ <https://gitlab.lam.fr/gyang/cigale/tree/xray>

Table 2. Properties of low-mass AGNs

Source #	ID _{L17}	ID _{G13}	RA (°)	Dec (°)	z	z -type	θ (')	C_{L17}	m_{F160W}	$\log(M_*)$	$\log(M_{*,err})$	ΔAIC
(1)	(2)	(3)	(4)	(5)	(6)	(7)	(8)	(9)	(10)	(11)	(12)	(13)
1	716	24716	53.15883	-27.66244	0.84	s	8.89	9399.8	20.00	9.59	0.63	1086.78
2	567	18955	53.12590	-27.75126	0.74	s	3.31	7393.2	21.10	9.87	0.11	1262.95
3	102	21937	53.00658	-27.72416	2.73	s	7.68	3250.2	22.60	9.76	0.60	155.74
4	252	6599	53.05835	-27.85018	0.12	s	4.12	3062.1	20.72	8.98	0.12	1347.90
5	449	26637	53.10485	-27.70521	1.62	s	6.09	2514.1	21.43	9.99	0.39	48.32
6	704	23708	53.15608	-27.66668	0.66	s	8.60	1702.6	21.13	9.89	0.14	173.19
7	788	14587	53.17848	-27.78402	3.19	s	3.48	1036.8	23.75	9.31	0.28	76.29
8	340	12338	53.07914	-27.79873	0.67	s	2.10	998.4	22.77	9.29	0.02	238.63
9	243	10323	53.05583	-27.81552	1.45	p	3.34	321.2	25.56	9.55	0.20	35.46
10	326	3643	53.07600	-27.87814	2.80	s	4.86	317.5	23.52	9.83	0.12	-6.25
⋮	⋮	⋮	⋮	⋮	⋮	⋮	⋮	⋮	⋮	⋮	⋮	⋮

NOTE—Column (1): source sequence number, assigned in order of descending net counts from L17. Columns (2) and (3): source ID in the L17 catalog and the CANDELS catalog, respectively. Columns (4) and (5): right ascension and declination in J2000 coordinates, respectively, taken from L17. Column (6): adopted redshift from L17. Column (7): type of redshift, with “s” meaning spectroscopic redshift and “p” referring to photometric redshift. Column (8): off-axis angle in units of arcminutes. Column (9): source’s net counts in the full band from the ACIS EXTRACT data products of the L17 catalog. Column (10): AB magnitude in the Hubble Space Telescope Wide Field Camera 3 (HST/WFC3) F160W filter, converted from the flux in the same filter given in the G13 catalog. Column (11) and (12): log stellar mass in units of solar masses and its corresponding uncertainty, measured by X-CIGALE. Column (13): difference in the Akaike Information Criterion (AIC) between the two models described in Section 3. The full table of 78 sources is available online in a machine-readable format.

young and old populations, as listed in Table 3. For galactic dust emission, we adopt the model from Dale et al. (2014) with $dM_{dust} \propto U^{-\alpha} dU$, in which M_{dust} is the dust mass, U is radiation-field intensity, and α is the slope. We only vary α and use the values of 1.0, 1.5, 2.0, and 2.5.

We adopt the SKIRTOR module (Stalevski et al. 2012, 2016) to compute the AGN UV-to-IR emission. The three free parameters for the SKIRTOR module are listed in Table 3. We allow the AGN fraction to vary since the AGN contribution may not be dominant for the sources in our sample. We set the viewing angle, θ , to 30° and 70° , which are the typical θ values for spectroscopic type 1 and type 2 AGNs, respectively (e.g., Yang et al. 2020; Ramos Padilla et al. 2022). Another free parameter is the color excess of the polar dust. We fix the other SKIRTOR parameters at their default values. For the X-ray module, we adopt the default values for the parameters.

To summarize, the parameters listed in Table 3 are the only ones allowed to vary, while the parameters not listed in Table 3 are fixed to their default values. For the fitting, we utilize the Bayesian-like analysis option supported by X-CIGALE, which provides the likelihood-weighted values of physical properties calculated, such as M_* . We obtain a total of 144 sources with $M_* \leq 10^{10} M_\odot$, while the remaining 447 sources have $M_* > 10^{10} M_\odot$. Among the low-mass sources, 78 of them are classified as AGNs and the remaining 66 are classified as normal galaxies. This SED-fitting procedure helps

us to fulfill the final criterion of our sample selection as described in Section 2.2.

Figure 1 shows the best-fit SEDs for two sources in our sample and Figure 2 shows a scatter plot of the stellar mass for the 591 sources fitted by X-CIGALE as a function of z . This study focuses on the subset of sources marked by cyan-colored stars located below the red dashed line, which are the 78 low-mass AGNs that fulfill all our selection criteria (see Section 2.2). In Figure 3, we compare the stellar masses measured by X-CIGALE to the stellar masses from Santini et al. (2015).² When running X-CIGALE we include an AGN component, whereas the stellar masses given by Santini et al. (2015) were estimated without considering AGN emission. As can be seen in Figure 3, the masses for the galaxy sample, denoted by purple dots, show good agreement between our and Santini et al. (2015) measurements. This agreement implies that we have run X-CIGALE robustly. Conversely, we can see a significant scatter in the stellar mass comparison for the AGN sample, denoted by cyan stars. This shows that the inclusion of an AGN component does affect the estimation of stellar mass and the AGN component is necessary when performing SED-fitting.

² Santini et al. (2015) provide stellar-mass estimates from different fitting methods carried out by various research groups. We adopt the median stellar mass from the estimates that include nebular emission in the model spectra, as it provides a relatively robust estimate, and because our X-CIGALE fitting also considers nebular emission.

Hence, for our sample, we adopt the stellar mass measured by X-CIGALE.

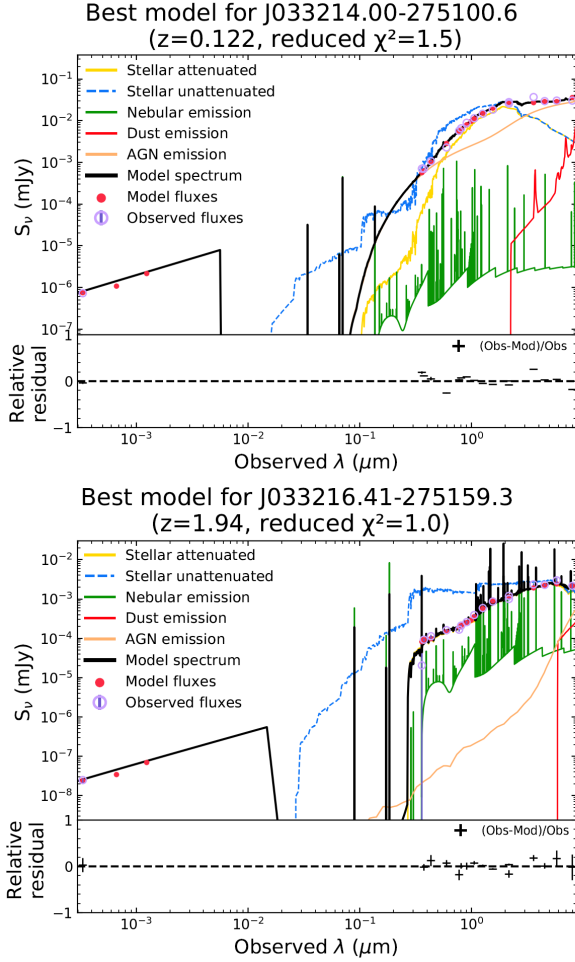


Figure 1. Examples of the SED fitting using X-CIGALE for sources #4 (top) and #13 (bottom). The fitting residuals (1 - model flux/observed flux) are shown at the bottom of each panel.

3. DATA PROCESSING AND ANALYSIS

3.1. Computing net photon flux for binned observations

In this work, we generate light curves using net photon flux, which is the net count rate per unit area in units of count $\text{s}^{-1} \text{cm}^{-2}$. The photon flux is derived from counts measured from the full-band photometry. We define total counts, C_{tot} , as the observed counts within the source aperture and background counts, C_{bkg} , as the observed counts within the background region. We scale C_{bkg} by the ratio of areas between the source and background regions to determine the background counts within the source aperture ($C_{\text{bkg, scaled}}$), accounting for the different sizes of the source and background regions. Finally, net counts, C_{net} , is the difference between the

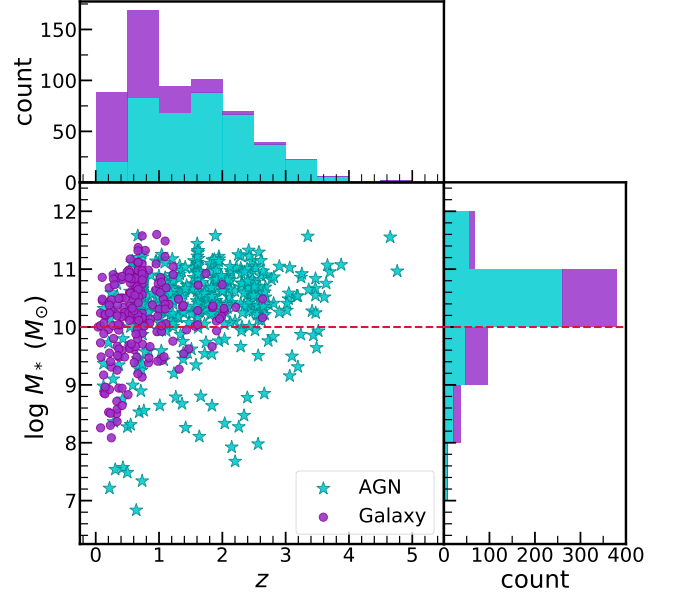


Figure 2. The stellar masses of the 591 sources fit by X-CIGALE are shown as a function of redshift. In the scatter plot, the cyan-colored stars indicate both the low- ($M_* \leq 10^{10} M_{\odot}$) and high-mass ($M_* > 10^{10} M_{\odot}$) AGNs, while the purple-colored dots indicate sources classified as galaxies, both in the low- and high-mass ranges. Above the scatter plot is a stacked redshift histogram and to the right of the scatter plot is a stacked histogram of M_* . In both panels, the cyan histogram represents AGNs in both mass ranges and the purple histogram includes both low- and high-mass galaxies. The red dashed lines denote the separation between low-mass and high-mass sources, at $M_* = 10^{10} M_{\odot}$.

total counts and the scaled background counts. The relation between these parameters is the following:

$$C_{\text{net}} = C_{\text{tot}} - C_{\text{bkg}} \times \frac{A_{\text{src}}}{A_{\text{bkg}}} = C_{\text{tot}} - C_{\text{bkg, scaled}} \quad (1)$$

where A_{src} is the area of the source region and A_{bkg} is the area of the background region. We use the inverse of the background scaling parameter (`backscal`) provided in the ACIS EXTRACT data products as the ratio of A_{src} to A_{bkg} .

We divide counts by the product of effective exposure in an epoch, E_{eff} , and point spread function (PSF) fraction of the source for the same epoch, f_{PSF} , to convert from counts to photon flux. The effective exposure is the product of effective exposure time and effective photon-collecting area of the telescope. The PSF is the response function of the telescope to a given point source; thus, the PSF fraction refers to the fraction of the counts from a point source enclosed by the detector's aperture. As an example of the conversion between counts and photon flux, we convert C_{net} to the observed net photon

Table 3. X-CIGALE Parameters

Module	Parameters	Values
Star formation history: Delayed model, $\text{SFR} \propto t \times \exp(-t/\tau)$	e -folding time, τ (Gyr) Stellar Age, t (Gyr)	0.1, 0.5, 1, 2, 5 0.5, 1, 3, 5, 7
Simple stellar population: Bruzual & Charlot (2003)	Initial mass function	Chabrier (2003)
Galactic dust attenuation: Calzetti et al. (2000) & Leitherer et al. (2002)	$E(B - V)$ ratio between the old and young populations $E(B - V)$ of starlight	1 0, 0.01, 0.02, 0.05, 0.1–0.5 (steps of 0.1), 0.7, 0.9
Galactic dust emission: Dale et al. (2014)	α slope in $dM_{\text{dust}} \propto U^{-\alpha} dU$	1.0, 1.5, 2.0, 2.5
AGN (UV-to-IR): SKIRTOR (Stalevski et al. 2012, 2016)	Viewing angle θ (face on: $\theta=0^\circ$, edge on: $\theta=90^\circ$) AGN fraction in total IR luminosity, f_{AGN} $E(B - V)$ of polar dust	30° (type 1), 70° (type 2) 0, 0.01, 0.1–0.9 (steps of 0.1), 0.99 0, 0.05, 0.1, 0.15, 0.2, 0.3
X-ray:	Maximum deviation from the $\alpha_{\text{ox}}-L_{2500\text{\AA}}$ relation	0.2

NOTE—X-CIGALE parameters not included here are set to their default values.

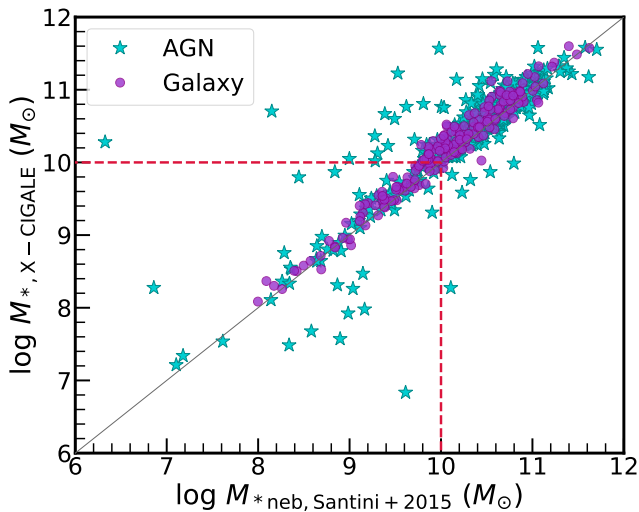


Figure 3. The comparison between the stellar mass from Santini et al. (2015) and the stellar mass as fitted by X-CIGALE. The figure shows a good agreement between the two sets of stellar masses for galaxies. The scatter in the stellar mass comparison for the AGNs implies that the inclusion of an AGN component (in X-CIGALE but not in Santini et al. (2015)) does affect mass estimation and is necessary for an accurate mass estimation. The red dashed lines denote the separation between low-mass and high-mass sources, at $M_* = 10^{10} M_\odot$.

flux, F_{net} , following the equation below:

$$F_{\text{net}} = \frac{C_{\text{net}}}{f_{\text{PSF}} \times E_{\text{eff}}} \quad (2)$$

All three parameters on the right-hand side of Equation 2 are obtained from the ACIS EXTRACT data products

from L17, which provide counts, effective exposure, and PSF fraction for each observation. Hence, merging observations into epochs requires either summing or averaging parameters from each observation to obtain values for an epoch. More specifically, C_{net} is the sum of net counts from all observations that comprise an epoch, while E_{eff} is the sum of the (average) effective exposure from each observation within an epoch, and f_{PSF} is the weighted average of the PSF fraction from the individual observations making up the epoch. As such, each source has five values of F_{net} , C_{net} , E_{eff} , and f_{PSF} , one for each epoch.

3.2. Fitting models to the light curve

In order to identify potential TDE candidates, we fit two different models to the light curves of sources in our sample – a TDE power-law model and a constant model. Below we describe the two models and the model fitting procedure.

3.2.1. The TDE Power-law and the Constant Models

To model the light curve of a TDE, we adopt a power law with an index of $-5/3$ because a power-law index of $-5/3$ (Rees 1988) is theoretically expected to describe the decline in X-ray emission for TDEs. We note that in Section 5, we relax this assumption and consider situations in which the net photon flux does not specifically decline as $t^{-5/3}$. The equation for the TDE power-law model is:

$$F_{\text{net,model}} = (t - t_0)^{-5/3} \times H(t - t_0) \times F_{\text{net,tde}} \quad (3)$$

where t_0 is the instance when a TDE starts to occur and $H(t - t_0)$ is the Heaviside step function. $H(t - t_0)$ takes

the value of unity only when $(t - t_0)$ is greater than zero and otherwise $H(t - t_0)$ is zero. This model has two free parameters, t_0 and $F_{\text{net,tde}}$, which is a normalization.

We set a lower limit for t_0 at $T = T_{\text{ep1}} - 10$, where T denotes rest-frame time in years and T_{ep1} is the rest-frame time of the first epoch. The lower limit on t_0 takes into consideration TDEs that may have happened in the past, up to 10 years before the first epoch. The motivation behind this lower limit is that the decay of the TDE emission often does not last for more than a decade (e.g., see Fig. 2 in Saxton et al. 2020).

We additionally fit the light curves with a constant model. The equation for the constant model is:

$$F_{\text{net,model}} = F_{\text{net,cst}} \quad (4)$$

with only one free parameter, $F_{\text{net,cst}}$.

3.2.2. Model Optimization

We fit the TDE power-law and constant models to the light curves using `scipy.optimize` to maximize the log-likelihood. We calculate the likelihood function for each model following the method detailed here. We use Poisson likelihood, which depends on C_{tot} and model total counts, $C_{\text{tot,model}}$. The latter requires us to determine the background photon flux, scaled by the ratio of areas between the source and background regions. The scaled background photon flux is:

$$F_{\text{bkg,scaled}} = \frac{C_{\text{bkg}}}{f_{\text{PSF}} \times E_{\text{eff}}} \times \frac{A_{\text{src}}}{A_{\text{bkg}}} = \frac{C_{\text{bkg,scaled}}}{f_{\text{PSF}} \times E_{\text{eff}}}. \quad (5)$$

From the models given in Equations 3 and 4, we obtain the model net photon flux, $F_{\text{net,model}}$. We then sum $F_{\text{net,model}}$ and $F_{\text{bkg,scaled}}$ to obtain the model total photon flux, $F_{\text{tot,model}}$. Next, we convert $F_{\text{tot,model}}$ to $C_{\text{tot,model}}$ as follows:

$$C_{\text{tot,model}} = F_{\text{tot,model}} \times (f_{\text{PSF}} \times E_{\text{eff}}). \quad (6)$$

We calculate the Poisson probability of the measured counts of each epoch using C_{tot} and $C_{\text{tot,model}}$ following

$$P(m, \lambda) = \frac{\lambda^m e^{-\lambda}}{m!} \quad (7)$$

where m is equal to C_{tot} and λ is equal to $C_{\text{tot,model}}$ for our case. For a given source, the likelihood for each model is the product of the Poisson probability of the five epochs, as shown below:

$$L = \prod_{i=1}^5 P_i \quad (8)$$

where the subscript of P refers to the i th epoch.

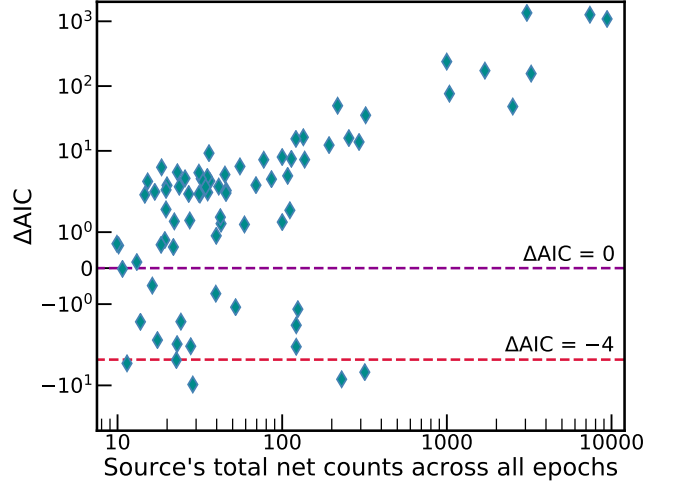


Figure 4. ΔAIC between the best-fit TDE power-law and constant models for the 78 sources as a function of total observed net counts in the 7 Ms exposure. The purple dashed line indicates where ΔAIC is 0 and the red dashed line indicates where ΔAIC is -4 . A majority of the sources have positive ΔAIC , implying that a constant model is preferred over the TDE model.

3.3. Model selection

After fitting both models to the light curves, we apply the Akaike information criterion (AIC; Akaike 1974) to compare the quality of the TDE and constant models relative to each other and to select the model with better support from the data. The AIC value of a model is defined as:

$$\text{AIC} = 2k - 2 \ln(L_{\text{max}}) \quad (9)$$

where k is the number of free parameters and L_{max} is the maximum value of the likelihood function of the fitted model. Our focus is on the difference in AIC between our two models, ΔAIC . Following Equation 9, ΔAIC is then defined as:

$$\Delta\text{AIC} = 2(k_T - k_C) - 2 \ln \left(\frac{L_{\text{max},T}}{L_{\text{max},C}} \right) \quad (10)$$

where the subscripts T and C refer to the TDE model and the constant model, respectively. The $(k_T - k_C)$ term is unity since we have two free parameters for the TDE model and one for the constant model. The ΔAIC between these two models for each source is listed in Table 2.

A negative value of ΔAIC indicates that the TDE model has a smaller value of AIC, and thus, is better supported by the data. A source with ΔAIC of -4 and lower indicates that the TDE model is considerably more supported than the constant model (Burnham & Anderson 2002). A ΔAIC of -4 corresponds to the source being 7 times more likely (Burnham & Anderson 2004) to

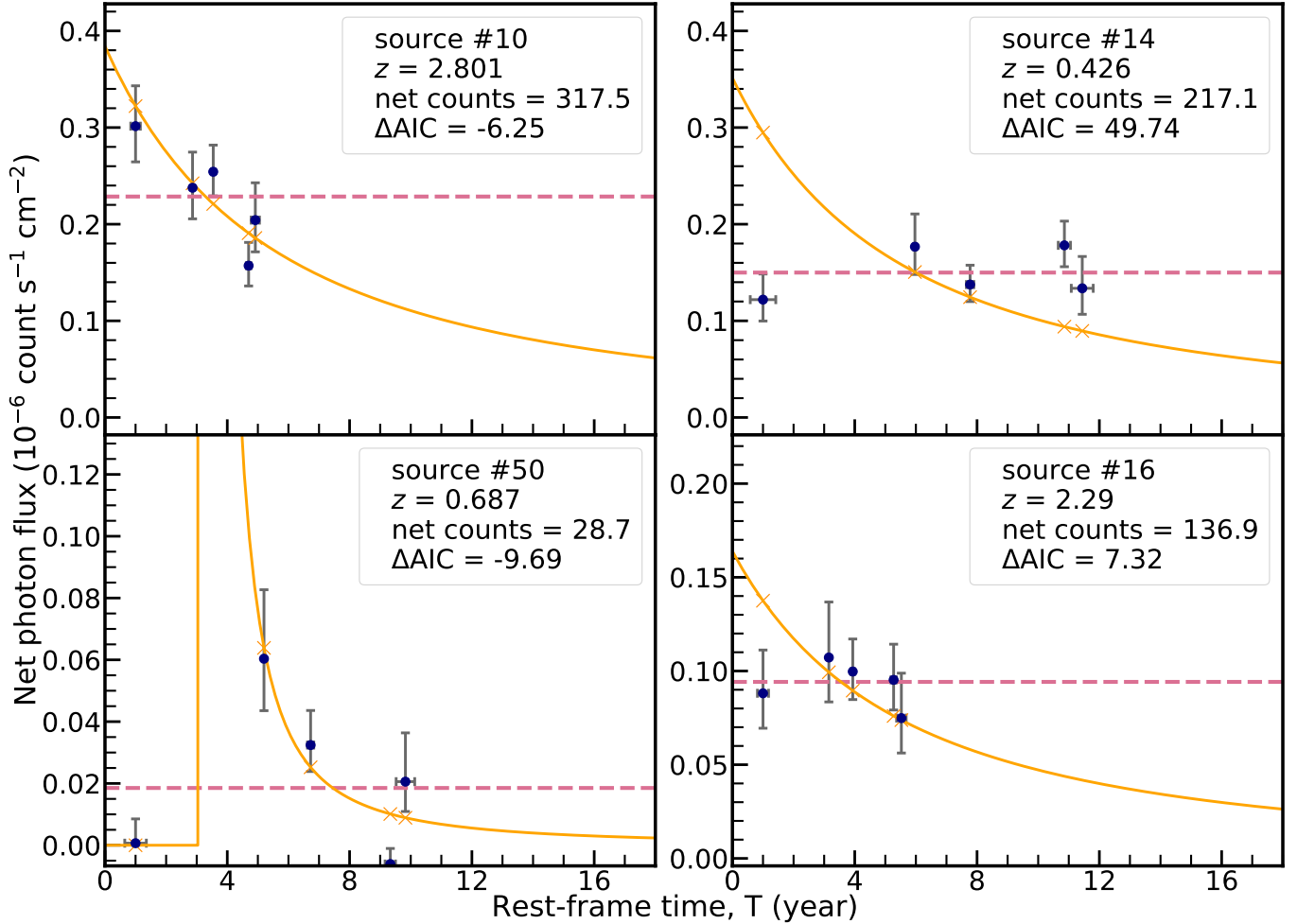


Figure 5. Light curves for four sources in our sample (blue dots), along with the best-fit TDE (orange solid curve) and constant (pink dashed line) models. The horizontal error bars indicate the bin width of each epoch, while the rest-frame time of the first epoch is set to year 1. The two sources on the left panels are two of the five TDE candidates, while the sources on the right panels are not TDE candidates. The other three TDE candidates not shown here have light curves and best-fit models similar to the candidates presented in the left panels. A few source properties are labelled on the panels, along with the ΔAIC between the two models. The net counts shown are C_{net} summed over all epochs.

be a TDE than not. Accordingly, a lower value of ΔAIC implies a higher likelihood of the source being a TDE. Thus, we impose $\Delta\text{AIC} < -4$ as an empirical criterion to select for TDE candidates and we find a total of 5 sources that satisfy this empirical threshold. Figure 4 displays the ΔAIC as a function of total observed net counts in the 7 Ms exposure for all 78 sources in the sample. As can be seen, the majority of the sources have positive ΔAIC , indicating that the data from these sources support the constant model better than the TDE model. Figure 5 shows the light curves of four sources and the best-fit models from the TDE power-law and constant models. These four sources are selected to show sources that prefer the TDE model as well as sources that prefer the constant model. In Figure 5, the two left panels show sources with a preference for the TDE model (neg-

ative values of ΔAIC), while the two right panels show sources with a preference for the constant model (positive ΔAIC values).

Based on ΔAIC , there are 5 TDE candidates in our sample. However, we emphasize that this does not necessarily mean all of them are bona-fide TDEs, as there might be false positives. In fact, not all 5 sources appear to be strong TDE candidates, based on visual inspection of their light curves and best-fit TDE models, as can be seen in the left panels of Figure 5. As ΔAIC is an empirical criterion, it is possible that a non-TDE-related event has been incorrectly selected as a TDE candidate based on its ΔAIC value, and vice versa. Thus, quantifying the TDE fraction, f_{TDE} , as the ratio of the number of TDE candidates to the total number of sources in our sample is not a robust approach. In Section 4,

we estimate the true-positive and false-positive rates for every source in the sample and use them to determine the Bayesian posterior of f_{TDE} .

4. CONSTRAINING THE TDE FRACTION

In order to constrain f_{TDE} , we need the true-positive rate and false-positive rate of each source. Here, we define true positive as the case where an actual TDE is categorized as a TDE, and false positive as the case in which the variability of an ordinary AGN is labelled as a TDE. To estimate the true-positive and false-positive rates of each source, we simulate artificial light curves of TDEs (see Section 4.1) and of ordinary AGNs (see Section 4.2) that correspond to each source’s net counts and redshift.

Using both the simulated TDE and ordinary AGN light curves, we apply a similar series of steps as explained in Section 3 to select for TDE candidates. The number of TDE candidates is then used to estimate the true- and false-positive rates for each source. From these true- and false-positive rates, we use a Bayesian analysis to estimate the posterior of the f_{TDE} for our sample (see Section 4.3).

4.1. Simulating TDE light curves

Our goal is to generate a light curve of simulated net photon flux, $F_{\text{net, sim}}$. $F_{\text{net, sim}}$ can be obtained from the difference between simulated total photon flux, $F_{\text{tot, sim}}$, and scaled simulated background photon flux, $F_{\text{bkg, scaled, sim}}$. We apply the following series of steps to calculate $F_{\text{tot, sim}}$. First, for a given low-mass source, we assign to t_0 an arbitrary value, ranging from $T_{\text{ep1}} - 10$ to T_{ep5} , drawn from a uniform distribution. With t_0 , we determine $F_{\text{net, tde}}$ using Equation 3 such that $C_{\text{net, model}}$ (converted from $F_{\text{net, model}}$ in Equation 3) summed over the five epochs, equals the C_{net} for a given source, summed over all five epochs. Thus, we can construct a model light curve ($F_{\text{net, model}}$ as a function of t) using the values of the $(t_0, F_{\text{net, tde}})$ pair. Next, following the steps in Section 3.2.2, we use $F_{\text{net, model}}$ and $F_{\text{bkg, scaled}}$ to obtain $F_{\text{tot, model}}$ and subsequently, $C_{\text{tot, model}}$. We then simulate total counts, $C_{\text{tot, sim}}$, from the Poisson distribution, using $C_{\text{tot, model}}$ as λ . We then convert $C_{\text{tot, sim}}$ to its flux counterpart, $F_{\text{tot, sim}}$, following Equation 2.

Computing $F_{\text{bkg, scaled, sim}}$ is straightforward. We first obtain simulated background counts, $C_{\text{bkg, sim}}$, from the Poisson distribution, using C_{bkg} as λ . Following Equation 1, we then scale $C_{\text{bkg, sim}}$ to obtain the scaled simulated background counts, $C_{\text{bkg, scaled, sim}}$. Next, we convert $C_{\text{bkg, scaled, sim}}$ to $F_{\text{bkg, scaled, sim}}$, following Equation 2. Lastly, we subtract $F_{\text{bkg, scaled, sim}}$ from $F_{\text{tot, sim}}$ to obtain $F_{\text{net, sim}}$, which forms a simulated light curve for

the source. The top two panels of Figure 6 present the simulated TDE light curve for two selected sources.

We now apply the maximum Poisson likelihood estimation as described in Section 3.2 to fit both models to the simulated light curve of $F_{\text{net, sim}}$. To achieve this, we use $C_{\text{tot, sim}}$ as m and $C_{\text{tot, model}}$ as λ for Equation 7. Following that, we determine the classification of the source as a TDE candidate or not, using the steps detailed in Section 3.3. For a given source, we repeat the series of steps as delineated above for a total of 1000 randomly generated t_0 . Lastly, we compute the true-positive rate for the source by tallying the number of iterations that identified the source as a TDE candidate and then dividing that tally by 1000.

The true-positive rate of the 78 sources in our sample is shown in the top panel of Figure 7, where it is plotted as a function of total observed net counts in the 7 Ms exposure. The colored stars refer to the five TDE candidates, while the colored dots are the non-candidates. The data points are also color-coded by the value of the source’s redshift. In general, at similar redshifts, the true-positive rate is higher for sources with higher net counts. This is because sources with higher net counts have higher statistical significance, which leads to a higher ability to reach the ΔAIC threshold to be considered a TDE candidate. At similar net counts, the true-positive rate is higher for sources with lower redshifts. Sources at lower redshifts have a longer baseline in the rest frame, which increases the probability of a TDE occurring during the baseline, making it easier to identify TDEs.

4.2. Simulating ordinary AGN light curves

Next, we generate model light curves of ordinary AGNs using the algorithm described in Emmanoulopoulos et al. (2013).³ In order to generate these model ordinary AGN light curves, we need known input parameters for the power spectral density (PSD) and the probability density function (PDF). PSD refers to the power of a time series as a function of frequency, while PDF refers to the probability distribution of the observed flux. For the PSD, we adopt the bending power law from Paolillo et al. (2017):

$$\text{PSD}(\nu) = \frac{A}{\nu} \left(\frac{1}{1 + \nu/\nu_b} \right) \quad (11)$$

³ Specifically, we use the PYTHON implementation by Connolly (2016), available from <https://github.com/samconnolly/DELightcurveSimulation>

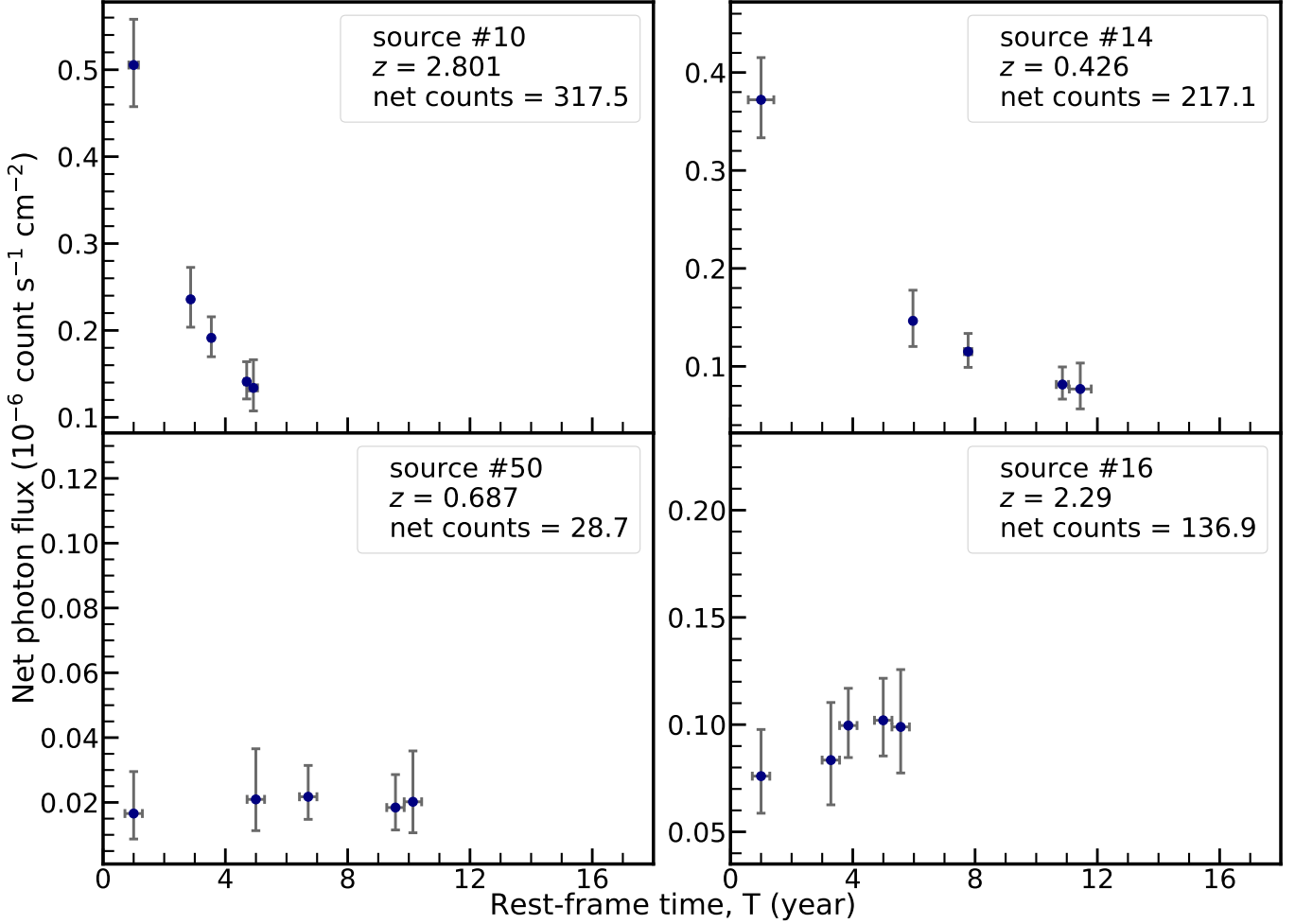


Figure 6. The top (bottom) two panels depict the simulated TDE (ordinary AGN) light curves for selected sources in our sample. In all four panels, the blue dots indicate the 5-epoch data points that form the light curves. The cyan-colored crosses in the bottom panels are the data points in the model ordinary AGN light curve that were not selected to form the simulated ordinary AGN light curves. Similar to Figure 5, the horizontal error bars indicate the bin width of each epoch. The rest-frame time of the first epoch is also set to year 1. Source properties such as redshift and net counts are labelled on the panels. The net counts shown are C_{net} summed over all epochs.

From Paolillo et al. (2017), we adopted a bending frequency, ν_b , of $5.8 \times 10^{-4} \text{ s}^{-1}$, and a normalization factor, A , of 0.04 s.

On the other hand, we adopt a lognormal distribution for the PDF. We need to estimate the dispersion for the PDF, thus we fit a log-normal distribution to the F_{net} of sources in the L17 catalog with $M_* > 10^{10} M_{\odot}$ and sum of C_{net} over five epochs > 500 . The counts cutoff is in place to ensure that the observations have high S/N and statistical significance. For the fitting, we focus on X-ray detected massive AGNs that are powered by cold-gas accretion, making them suitable analogs for the ordinary AGNs in the dwarf galaxy sample. We obtain a dispersion of 0.1109 dex.

Each model light curve has 36 data points, with an interval of 0.57 years, making the duration of the entire

light curve approximately 20.5 years. We choose this light-curve duration as it is long enough to cover the rest-frame light curve of all sources. We also use the median bin width of our observed epochs (refer to Table 1) as the interval of our model light curve. Next, we want to identify the data points that will be used to form the 5-epoch ordinary AGN light curves. As the model light curve is generated in the rest frame, we converted the observed timestamps for every source from the observed frame to the rest frame. Then, we identify the data point of the model light curve closest to each of the rest-frame timestamp. Therefore, for each of the model light curve, there are 5 data points, one for each epoch, similar to the observed light curve.

The model ordinary AGN light curve is in the form of net photon flux, $F_{\text{net,model}}$; thus, we use Equation 2

to convert $F_{\text{net,model}}$ to $C_{\text{net,model}}$. We then normalize the light curve by the ratio of the sum of $C_{\text{net,model}}$ to the sum of C_{net} . This normalization factor adjusts the light curve so that the model net counts correspond to the observed net counts of the source.

We generate 1000 model ordinary AGN light curves for each source as elaborated above. For every light curve, similar to the steps in Section 3.2.2, we sum $F_{\text{net,model}}$ and $F_{\text{bkg,scaled}}$ to get $F_{\text{tot,model}}$. We then convert $F_{\text{tot,model}}$ to $C_{\text{tot,model}}$ using Equation 2. Next, we obtain $C_{\text{tot,sim}}$ from the Poisson distribution, using $C_{\text{tot,model}}$ as λ . $C_{\text{tot,sim}}$ is then converted to $F_{\text{tot,sim}}$. On the other hand, $F_{\text{bkg,scaled,sim}}$ is calculated following the same steps as delineated in Section 4.1. Lastly, we obtained $F_{\text{net,sim}}$ by subtracting $F_{\text{bkg,scaled,sim}}$ from $F_{\text{tot,sim}}$. We now obtain simulated light curves of ordinary AGNs, 1000 for each source. In Figure 6, the bottom two panels display the simulated ordinary AGN light curves for two sources.

We proceed to fit the TDE and constant models to each of the simulated ordinary AGN light curves using maximum Poisson likelihood estimation as explained in Section 3.2, and then determine if the source is a TDE candidate, following the steps explained in Section 3.3. Lastly, we compute the false-positive rate from the 1000 simulated ordinary AGN light curves — we sum up the number of iterations that classified the source as a TDE candidate, and then divide the sum by 1000 to obtain the false-positive rate for the source.

The false-positive rate of the sources in our sample is shown in the bottom panel of Figure 7. In general, at similar net counts, the false-positive rate is higher when the source’s redshift is higher, although it is only noticeable for sources with high net counts. At lower (< 100) net counts, the false-positive rate is similar regardless of redshift. There is also a noticeably large dispersion in the false-positive rate for high-count sources. This is likely due to the higher probability of misidentifying ordinary AGNs as TDEs at higher redshift and shorter observation baseline. On the other hand, at any given redshift, the false-positive rate is generally lower for sources with lower net counts. This is similar to the trend of the true-positive rate being lower for sources with lower net counts at similar redshifts. Sources with lower net counts have lower statistical significance, which decreases their ability to meet the ΔAIC threshold to be classified as a TDE candidate, thus lowering the false-positive rate.

4.3. Posterior of the TDE fraction

Here, using both the true- and false-positive rates, we apply Bayesian analysis to estimate the f_{TDE} posterior

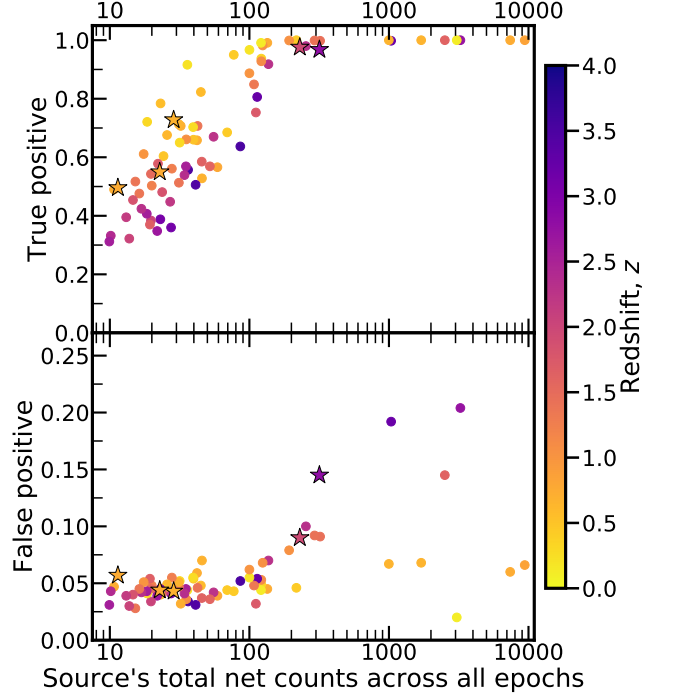


Figure 7. The top (bottom) panel shows the true (false)-positive rate of the sources as a function of their sum of net counts. Colored stars indicate the TDE candidates in our sample, while the colored dots are non-candidates. The data points are color-coded by their redshifts — yellow tones are used for low redshifts, and purple tones are used for higher redshifts. In general, both true- and false-positive rates increase with net counts at any given redshifts. At a given net count, the true-positive rate is higher for sources with lower redshifts, while the false-positive rate is higher for sources with higher redshifts. Note that the two panels have different limits on the y-axis.

from our dataset. We use Bayes’ theorem:

$$p(\theta|D) = \frac{p(\theta)p(D|\theta)}{p(D)} \quad (12)$$

where $p(D)$ refers to the evidence, and is a constant independent of data. We note that $p(\theta)$ is the prior probability that the model parameter, θ , or in our case f_{TDE} , takes on a specific value. For our analysis, we assume a flat prior, therefore, $p(\theta)$, or $p(f_{\text{TDE}})$ is assumed to be a constant. This simplifies Equation 12 into:

$$p(f_{\text{TDE}}|D) \propto \frac{p(D|f_{\text{TDE}})}{p(D)} \quad (13)$$

where $p(f_{\text{TDE}}|D)$ is the posterior probability distribution, or the probability of getting a certain value of f_{TDE} , given the condition that 5/78 sources in our sample are selected as TDE candidates. Lastly, $p(D|f_{\text{TDE}})$ refers to the probability of selecting 5/78 sources as TDE candidates given a f_{TDE} .

Our goal is to compute $p(f_{\text{TDE}}|D)$. We determine $p(f_{\text{TDE}}|D)$ using a Monte Carlo simulation and we first compute $p(D|f_{\text{TDE}})$. We define the range of f_{TDE} from $0/78$ to $78/78$, at an interval of $1/78$. For every f_{TDE} , we randomly assign $N_{\text{TDE}} = f_{\text{TDE}} \times 78$ sources as TDEs in the sample. The probability of a source being chosen as a TDE depends on whether it was designated as a TDE or not. If a source is assigned as a TDE, its probability of being selected as a TDE is its true-positive rate. Conversely, if the source is designated as a non-TDE, its probability of being selected as a TDE corresponds to its false-positive rate. We apply the following steps to ‘select’ TDEs from our sample. We first draw a random number, ranging from 0 to 1, from a uniform distribution. If the number drawn is less than the true-positive rate for a source designated as a TDE (or false-positive rate for an assigned non-TDE), the source is then ‘selected’ randomly as a TDE. Then, at a given f_{TDE} , we run 100000 Monte Carlo simulations to select TDEs from the sample. We tally the number of iterations for each f_{TDE} that selects exactly 5 sources as TDEs and divide it by 100000. This gives us $p(D|f_{\text{TDE}})$.

Then, we divide $p(D|f_{\text{TDE}})$ by the total number of iterations with exactly 5 sources selected as TDEs across all values of f_{TDE} . This gives us $p(f_{\text{TDE}}|D)$. Finally, we normalize $p(f_{\text{TDE}}|D)$ such that its integral equals to unity, as shown in Equation 14:

$$\int_{-\infty}^{\infty} p(f_{\text{TDE}}|D) df_{\text{TDE}} = 1 \quad (14)$$

Figure 8 shows the posterior, i.e. the normalized $p(f_{\text{TDE}}|D)$. The peak of the posterior is 2.56%, which is very close to zero. We also obtain a 2- σ upper limit of 9.80%.

5. DISCUSSION

In Section 4.3, we showed that the posterior f_{TDE} peaks close to zero (2.56%) with an upper limit of 9.80%. Thus, most AGNs in dwarf galaxies in our dataset are likely *not* TDE-powered and black-hole growth via the TDE channel may be insignificant. However, our previous analyses assume that TDE light curves follow a canonical form of $t^{-5/3}$. In this section, we supplement our analyses with sanity checks that do not rely on such an assumption.

First, we search for large changes in flux between pairs of epochs for each source. In this way, we are able to identify possible TDEs, which would produce large deviations from a unity flux ratio, without assuming a particular form for the light curve.

Figure 9 compares F_{net} between epochs 1 and 5 (left column) and between epochs 3 and 4 (right column)

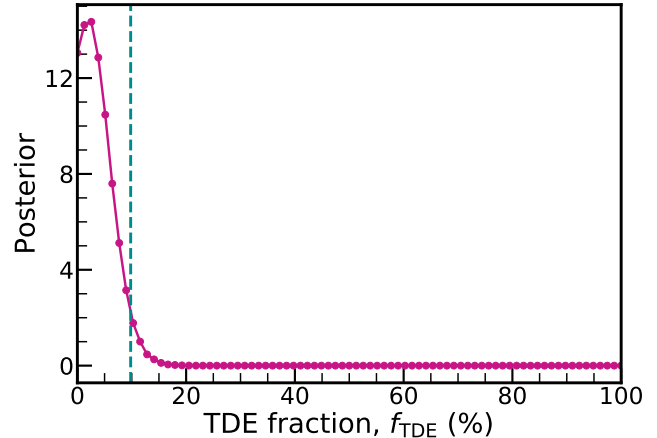


Figure 8. Posterior of f_{TDE} . The distribution peaks at $f_{\text{TDE}} = 2.56\%$ and rapidly decreases to 0. The dashed line marks the 2- σ upper limit of the posterior, which occurs at $f_{\text{TDE}} = 9.80\%$.

as examples. The top two panels each show how the F_{net} of two epochs compare to each other. Nearly all 78 sources show less than a factor of two change in flux. This indicates that there are no extreme changes in flux between epochs (a key signature of TDEs). The bottom two panels each show the distribution of the logarithmic values of the F_{net} ratios of two epochs. The median of the distribution, indicated by the blue dashed vertical line, is close to zero. The other eight pairs of epochs not shown here show similar results. The flux vs. flux properties above are consistent with the behavior of ordinary AGNs in general (e.g., Yang et al. 2016), disfavoring the claim that our sample is predominantly TDEs.

We use another diagnostic to assess whether our sources are TDE candidates – we inspect the effective power-law photon index, Γ , of the sources.⁴ These Γ values are adopted from L17. This is motivated by the fact that TDEs and ordinary AGNs typically have very different values of Γ . Figure 10 shows the Γ distribution of our sample. We note that 47 sources are excluded from the distribution because they are undetected in the soft and/or hard bands, and thus, their values of Γ cannot be effectively constrained. The distribution of Γ has a peak between $\Gamma \sim 1.25$ and $\Gamma=2$. This peak disagrees with the typical nature of the soft X-ray emission from a typical (or non-jetted) TDE, which often has $\Gamma \gtrsim 4$ (e.g., Ghosh et al. 2006; Auchettl et al. 2017; Saxton

⁴ Admittedly, fitting a more complex model such as a blackbody + power-law model could be more ideal for TDE identification. Unfortunately, our sources generally have limited numbers of counts (median counts = 40), preventing us from employing more complex models.

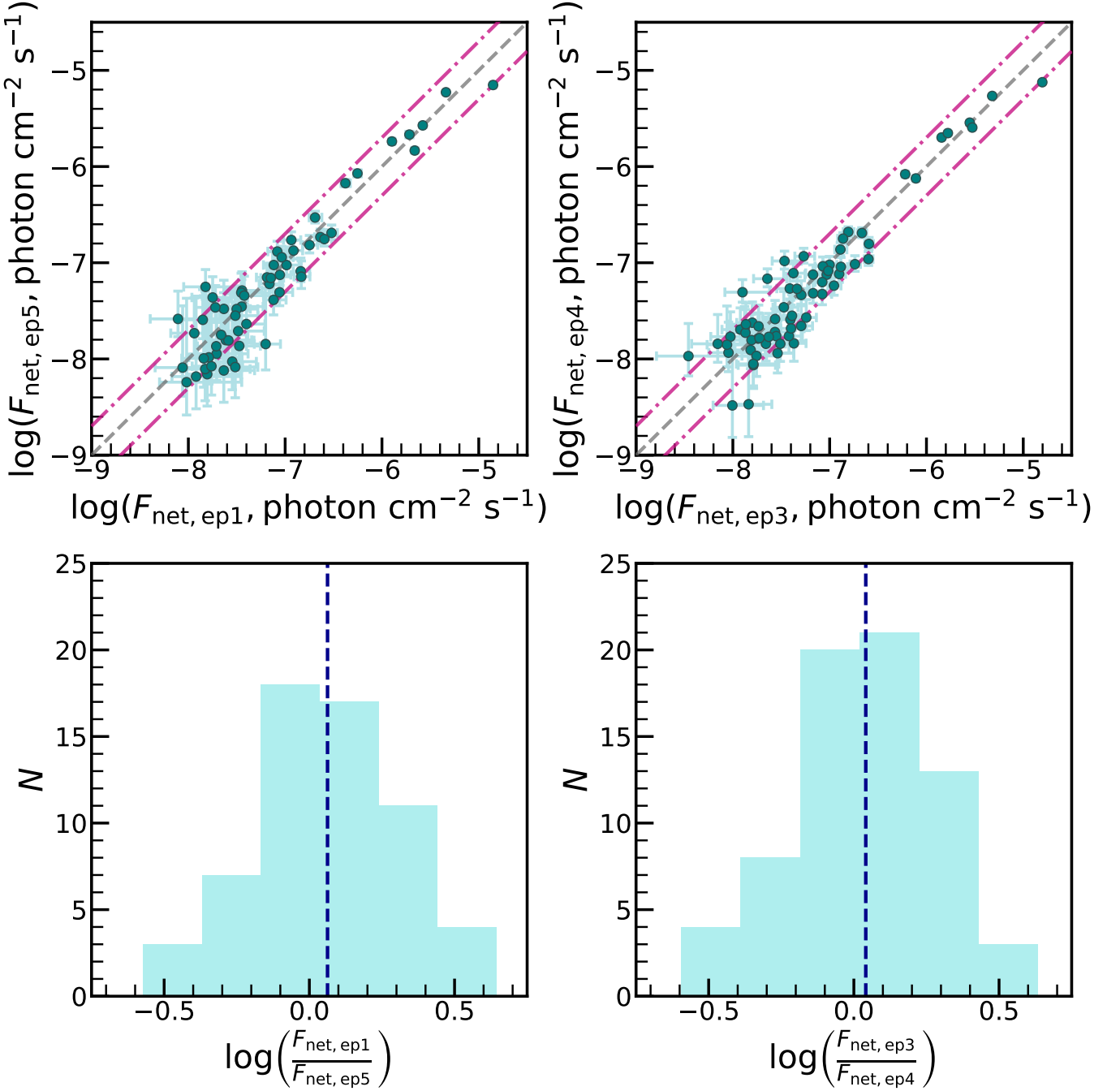


Figure 9. The top two panels show the comparison of full-band net photon fluxes between epochs 1 and 5 (left panel), and between epochs 3 and 4 (right panel). The grey dashed line of unity indicates no change in flux between epochs; the pink dash-dot lines indicate flux changes of a factor of two. The fluxes between epochs are similar to within a factor of two for most sources in our sample. The bottom two panels show the distribution of the log values of the flux ratios between epochs (same pairs as the top panels). The blue dashed vertical line denotes the median of the distribution. The median log flux ratio and the location of the peak of the distribution are consistent with zero, indicating that there are no systematic changes in flux between epochs.

et al. 2020; Sazonov et al. 2021).⁵ In contrast, the peak is similar to the X-ray emission from an ordinary AGN, which typically has intrinsic $\Gamma \sim 1.8$ (e.g., Tozzi et al. 2006; Marchesi et al. 2016; Auchettl et al. 2018).⁶ Thus, based on their Γ values, it is unlikely that the sources in our sample are predominantly TDEs. Even for the TDE candidates (pink histograms in Figure 10) identified in Section 3, their Γ values are all < 3 , suggesting that they are actually false positives.

We emphasize that the two diagnostics performed here are primarily qualitative in nature. They serve as a sanity checks, i.e., to strengthen our main conclusion that most of our sources are not TDEs.

Some TDEs could be partial TDEs (PTDEs), and the PTDE decay follows $t^{-9/4}$ instead of $t^{-5/3}$ (e.g., Coughlin & Nixon 2019; Miles et al. 2020). Here, we address the concern that fitting a $t^{-5/3}$ model to PTDEs may lead to incorrect conclusions. We simulated PTDE light curves following Section 4.1 by replacing the power-law index of $-5/3$ with $-9/4$. We then fit the $t^{-5/3}$ and constant models to the simulated PTDE light curves to compute the true-positive rates for the sources. We subsequently use the true- and false-positive rates to estimate the f_{TDE} posterior. We find that the posterior is consistent with the posterior calculated in Section 4.3. The old and new posteriors peak at similar f_{TDE} values (2.56% and 1.28%) and have similar $2\text{-}\sigma$ upper limits (9.80% and 8.24%). This finding indicates that our main conclusion remains qualitatively the same (i.e., most of our sources are ordinary AGNs rather than TDEs), even if the TDE decay power-law index is slightly different from $-5/3$.

6. SUMMARY AND FUTURE PROSPECTS

In this paper, we systematically search for TDEs among the X-ray detected AGNs in dwarf galaxies from the 7 Ms CDF-S survey. To select dwarf galaxies with $M_* \leq 10^{10} M_\odot$, we perform SED fitting for the X-ray sources in the CANDELS region, using X-CIGALE (§2). We end up with a sample of 78 low-mass AGNs. We extract the 16-year (observed-frame) light curves for our selected sources (§3). To enhance S/N, the light curves are binned into five epochs, each having $\approx 1\text{--}2$ Ms ex-

⁵ X-ray emission from TDEs with relativistic jets has a typical Γ value of $\sim 1\text{--}2$. However, results from previous studies (e.g., Bower 2011; Bower et al. 2013; Brown et al. 2015) state that only $\sim 10\%$ of TDEs are jetted.

⁶ We note that 1.8 is the typical intrinsic (without obscuration) value of Γ for X-ray emission from ordinary AGNs. However, obscuration can lead to harder X-ray emission, lowering the effective value of Γ . AGN obscuration and statistical uncertainties are likely the causes for some sources having $\Gamma \leq 1$.

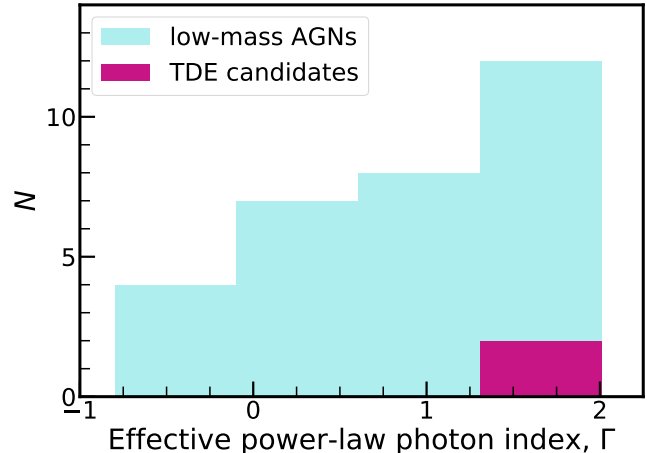


Figure 10. Distribution of the effective power-law photon index, Γ , of sources in our sample. Our sources are not TDE-dominated as none of them have Γ that is typical of TDEs. The peak of the Γ distribution for the TDE candidates (pink histogram) is at ~ 1.75 , agreeing with the peak of the distribution for the full sample (light blue histogram). The Γ distribution for the TDE candidates disagrees with the value of Γ typical of TDEs. As such, the TDE candidates are unlikely to be real TDEs.

posure. We then fit two models, the TDE power-law model and the constant model, to the light curves. We compare the two models using the AIC statistic, and consider sources with $\Delta\text{AIC} < -4$ as potential TDE candidates. There are a total of 5 sources with $\Delta\text{AIC} < -4$.

We constrain the TDE fraction by simulating both the TDE and ordinary AGN light curves to obtain true- and false-positive rates for each source (§4). We then use these rates and a Bayesian approach to obtain the posterior for the TDE fraction of our observed dataset. From the posterior, we obtain an upper limit of 9.80% for f_{TDE} . This low value of the TDE fraction does not support the claim that AGNs in dwarf galaxies are predominantly powered by TDEs (e.g., Zubovas 2019).

We compared F_{net} between pairs of epochs to detect large changes in flux and search for possible TDEs in a model-independent way. We found that the changes in flux for most sources are within a factor of two across all pairs of epochs. This small change in flux suggests that the light curves are unlikely the result of a TDE. We also performed sanity checks based on the flux ratios between epoch pairs and Γ values (§5). These qualitative analyses also suggest that most of our sources are ordinary AGNs rather than TDEs, supporting our main conclusion.

Nevertheless, the sample size of 78 sources in this work is limited. The multi-year surveys from eROSITA and *Athena* will be suitable to probe large samples of sources

to better constrain f_{TDE} among AGNs in dwarf galaxies. *Athena* has a large photon-collecting area, enabling more effective deep surveys. A substantial number of fainter sources could be observed with reasonable S/N, increasing the sample size of sources that would be useful for long-term X-ray variability studies. eROSITA, thanks to its large field of view, can hunt for TDEs among nearby dwarf galaxies across the entire sky and is expected to. Khabibullin et al. (2014) predicted that eROSITA could detect up to several thousands of TDE candidates during its all-sky survey, while Sazonov et al. (2021) updated the prediction to ~ 700 TDEs. On top of that, out of the 13 TDEs from the first *SRG*/eROSITA TDE sample, five of them are hosted by dwarf galaxies (see Appendix C of Sazonov et al. (2021) for details on the host galaxies' properties). eROSITA's expected yield of AGNs on the order of millions will also be helpful in constraining f_{TDE} in low-mass galaxies.

ACKNOWLEDGMENTS

We thank the referee for helpful feedback that improved this work. GY acknowledges funding from the Netherlands Research School for Astronomy (NOVA). WNB acknowledges support from NSF grants AST-2106990 and AST-2407089 and the Penn State Eberly Endowment. BL acknowledges financial support from the National Natural Science Foundation of China grant 11991053. YQX acknowledges support from the National Natural Science Foundation of China (NSFC-12025303, 11890693). This research has made use of

Software: Astropy (Astropy Collaboration et al. 2013, 2018, 2022), Matplotlib (Hunter 2007), SciPy (Virtanen et al. 2020), NumPy (Harris et al. 2020), X-CIGALE (Boquien et al. 2019; Yang et al. 2020)

Facility: CXO

REFERENCES

- Akaike, H. 1974, IEEE Trans. Automatic Control, AC-19, 716, doi: [10.1109/tac.1974.1100705](https://doi.org/10.1109/tac.1974.1100705)
- Astropy Collaboration, Robitaille, T. P., Tollerud, E. J., et al. 2013, A&A, 558, A33, doi: [10.1051/0004-6361/201322068](https://doi.org/10.1051/0004-6361/201322068)
- Astropy Collaboration, Price-Whelan, A. M., Sipőcz, B. M., et al. 2018, AJ, 156, 123, doi: [10.3847/1538-3881/aabc4f](https://doi.org/10.3847/1538-3881/aabc4f)
- Astropy Collaboration, Price-Whelan, A. M., Lim, P. L., et al. 2022, ApJ, 935, 167, doi: [10.3847/1538-4357/ac7c74](https://doi.org/10.3847/1538-4357/ac7c74)
- Auchettl, K., Guillochon, J., & Ramirez-Ruiz, E. 2017, ApJ, 838, 149, doi: [10.3847/1538-4357/aa633b](https://doi.org/10.3847/1538-4357/aa633b)
- Auchettl, K., Ramirez-Ruiz, E., & Guillochon, J. 2018, ApJ, 852, 37, doi: [10.3847/1538-4357/aa9b7c](https://doi.org/10.3847/1538-4357/aa9b7c)
- Bauer, F. E., Treister, E., Schawinski, K., et al. 2017, MNRAS, 467, 4841, doi: [10.1093/mnras/stx417](https://doi.org/10.1093/mnras/stx417)
- Boquien, M., Burgarella, D., Roehly, Y., et al. 2019, A&A, 622, A103, doi: [10.1051/0004-6361/201834156](https://doi.org/10.1051/0004-6361/201834156)
- Bower, G. C. 2011, ApJL, 732, L12, doi: [10.1088/2041-8205/732/1/L12](https://doi.org/10.1088/2041-8205/732/1/L12)
- Bower, G. C., Metzger, B. D., Cenko, S. B., Silverman, J. M., & Bloom, J. S. 2013, ApJ, 763, 84, doi: [10.1088/0004-637X/763/2/84](https://doi.org/10.1088/0004-637X/763/2/84)
- Broos, P. S., Townsley, L. K., Feigelson, E. D., et al. 2010, ApJ, 714, 1582, doi: [10.1088/0004-637X/714/2/1582](https://doi.org/10.1088/0004-637X/714/2/1582)
- Brown, G. C., Levan, A. J., Stanway, E. R., et al. 2015, MNRAS, 452, 4297, doi: [10.1093/mnras/stv1520](https://doi.org/10.1093/mnras/stv1520)
- Bruzual, G., & Charlot, S. 2003, MNRAS, 344, 1000, doi: [10.1046/j.1365-8711.2003.06897.x](https://doi.org/10.1046/j.1365-8711.2003.06897.x)
- Burnham, K. P., & Anderson, D. R., eds. 2002, Information and Likelihood Theory: A Basis for Model Selection and Inference (New York, NY: Springer New York), 49–97, doi: [10.1007/978-0-387-22456-5_2](https://doi.org/10.1007/978-0-387-22456-5_2)
- Burnham, K. P., & Anderson, D. R. 2004, Sociological Methods & Research, 33, 261, doi: [10.1177/0049124104268644](https://doi.org/10.1177/0049124104268644)
- Calzetti, D., Armus, L., Bohlin, R. C., et al. 2000, ApJ, 533, 682, doi: [10.1086/308692](https://doi.org/10.1086/308692)
- Chabrier, G. 2003, ApJL, 586, L133, doi: [10.1086/374879](https://doi.org/10.1086/374879)
- Connolly, S. D. 2016, DELightcurveSimulation: Light curve simulation code. <http://ascl.net/1602.012>
- Coughlin, E. R., & Nixon, C. J. 2019, ApJL, 883, L17, doi: [10.3847/2041-8213/ab412d](https://doi.org/10.3847/2041-8213/ab412d)
- Dale, D. A., Helou, G., Magdis, G. E., et al. 2014, ApJ, 784, 83, doi: [10.1088/0004-637X/784/1/83](https://doi.org/10.1088/0004-637X/784/1/83)
- Elbaz, D., Dickinson, M., Hwang, H. S., et al. 2011, A&A, 533, A119, doi: [10.1051/0004-6361/201117239](https://doi.org/10.1051/0004-6361/201117239)
- Emmanoulopoulos, D., McHardy, I. M., & Papadakis, I. E. 2013, MNRAS, 433, 907, doi: [10.1093/mnras/stt764](https://doi.org/10.1093/mnras/stt764)
- Fischer, J. U., Hasinger, G., Schwobe, A. D., et al. 1998, Astronomische Nachrichten, 319, 347, doi: [10.1002/asna.2123190603](https://doi.org/10.1002/asna.2123190603)
- Garmire, G. P., Bautz, M. W., Ford, P. G., Nousek, J. A., & Ricker, George R., J. 2003, in Society of Photo-Optical Instrumentation Engineers (SPIE) Conference Series, Vol. 4851, X-Ray and Gamma-Ray Telescopes and Instruments for Astronomy., ed. J. E. Truemper & H. D. Tananbaum, 28–44, doi: [10.1117/12.461599](https://doi.org/10.1117/12.461599)

- Ghosh, K. K., Suleymanov, V., Bikmaev, I., Shimansky, S., & Sakhbullin, N. 2006, MNRAS, 371, 1587, doi: [10.1111/j.1365-2966.2006.10723.x](https://doi.org/10.1111/j.1365-2966.2006.10723.x)
- Greene, J. E., Strader, J., & Ho, L. C. 2020, ARA&A, 58, 257, doi: [10.1146/annurev-astro-032620-021835](https://doi.org/10.1146/annurev-astro-032620-021835)
- Guo, Y., Ferguson, H. C., Giavalisco, M., et al. 2013, ApJS, 207, 24, doi: [10.1088/0067-0049/207/2/24](https://doi.org/10.1088/0067-0049/207/2/24)
- Harris, C. R., Millman, K. J., van der Walt, S. J., et al. 2020, Nature, 585, 357, doi: [10.1038/s41586-020-2649-2](https://doi.org/10.1038/s41586-020-2649-2)
- Hunter, J. D. 2007, Computing in Science & Engineering, 9, 90, doi: [10.1109/MCSE.2007.55](https://doi.org/10.1109/MCSE.2007.55)
- Khabibullin, I., Sazonov, S., & Sunyaev, R. 2014, MNRAS, 437, 327, doi: [10.1093/mnras/stt1889](https://doi.org/10.1093/mnras/stt1889)
- Kormendy, J., & Ho, L. C. 2013, ARA&A, 51, 511, doi: [10.1146/annurev-astro-082708-101811](https://doi.org/10.1146/annurev-astro-082708-101811)
- Leitherer, C., Li, I. H., Calzetti, D., & Heckman, T. M. 2002, ApJS, 140, 303, doi: [10.1086/342486](https://doi.org/10.1086/342486)
- Lin, D., Carrasco, E. R., Grupe, D., et al. 2011, ApJ, 738, 52, doi: [10.1088/0004-637X/738/1/52](https://doi.org/10.1088/0004-637X/738/1/52)
- Lin, D., Strader, J., Carrasco, E. R., et al. 2018, MNRAS, 474, 3000, doi: [10.1093/mnras/stx2940](https://doi.org/10.1093/mnras/stx2940)
- Luo, B., Brandt, W. N., Xue, Y. Q., et al. 2017, ApJS, 228, 2, doi: [10.3847/1538-4365/228/1/2](https://doi.org/10.3847/1538-4365/228/1/2)
- Magorrian, J., & Tremaine, S. 1999, MNRAS, 309, 447, doi: [10.1046/j.1365-8711.1999.02853.x](https://doi.org/10.1046/j.1365-8711.1999.02853.x)
- Maksym, W. P., Lin, D., & Irwin, J. A. 2014, ApJL, 792, L29, doi: [10.1088/2041-8205/792/2/L29](https://doi.org/10.1088/2041-8205/792/2/L29)
- Marchesi, S., Lanzuisi, G., Civano, F., et al. 2016, ApJ, 830, 100, doi: [10.3847/0004-637X/830/2/100](https://doi.org/10.3847/0004-637X/830/2/100)
- Miles, P. R., Coughlin, E. R., & Nixon, C. J. 2020, ApJ, 899, 36, doi: [10.3847/1538-4357/ab9c9f](https://doi.org/10.3847/1538-4357/ab9c9f)
- Paolillo, M., Papadakis, I., Brandt, W. N., et al. 2017, MNRAS, 471, 4398, doi: [10.1093/mnras/stx1761](https://doi.org/10.1093/mnras/stx1761)
- Predehl, P., Andritschke, R., Arefiev, V., et al. 2021, A&A, 647, A1, doi: [10.1051/0004-6361/202039313](https://doi.org/10.1051/0004-6361/202039313)
- Ramos Padilla, A. F., Wang, L., Malek, K., Efstathiou, A., & Yang (杨光), G. 2022, MNRAS, 510, 687, doi: [10.1093/mnras/stab3486](https://doi.org/10.1093/mnras/stab3486)
- Rees, M. J. 1988, Nature, 333, 523, doi: [10.1038/333523a0](https://doi.org/10.1038/333523a0)
- Santini, P., Ferguson, H. C., Fontana, A., et al. 2015, ApJ, 801, 97, doi: [10.1088/0004-637X/801/2/97](https://doi.org/10.1088/0004-637X/801/2/97)
- Saxton, R., Komossa, S., Auchettl, K., & Jonker, P. G. 2020, SSRv, 216, 85, doi: [10.1007/s11214-020-00708-4](https://doi.org/10.1007/s11214-020-00708-4)
- Sazonov, S., Gilfanov, M., Medvedev, P., et al. 2021, MNRAS, 508, 3820, doi: [10.1093/mnras/stab2843](https://doi.org/10.1093/mnras/stab2843)
- Stalevski, M., Fritz, J., Baes, M., Nakos, T., & Popović, L. Č. 2012, MNRAS, 420, 2756, doi: [10.1111/j.1365-2966.2011.19775.x](https://doi.org/10.1111/j.1365-2966.2011.19775.x)
- Stalevski, M., Ricci, C., Ueda, Y., et al. 2016, MNRAS, 458, 2288, doi: [10.1093/mnras/stw444](https://doi.org/10.1093/mnras/stw444)
- Stone, N. C., & Metzger, B. D. 2016, MNRAS, 455, 859, doi: [10.1093/mnras/stv2281](https://doi.org/10.1093/mnras/stv2281)
- Sunyaev, R., Arefiev, V., Babyshkin, V., et al. 2021, A&A, 656, A132, doi: [10.1051/0004-6361/202141179](https://doi.org/10.1051/0004-6361/202141179)
- Tozzi, P., Gilli, R., Mainieri, V., et al. 2006, A&A, 451, 457, doi: [10.1051/0004-6361:20042592](https://doi.org/10.1051/0004-6361:20042592)
- Virtanen, P., Gommers, R., Oliphant, T. E., et al. 2020, Nature Methods, 17, 261, doi: [10.1038/s41592-019-0686-2](https://doi.org/10.1038/s41592-019-0686-2)
- Wang, J., & Merritt, D. 2004, ApJ, 600, 149, doi: [10.1086/379767](https://doi.org/10.1086/379767)
- Xue, Y. Q. 2017, NewAR, 79, 59, doi: [10.1016/j.newar.2017.09.002](https://doi.org/10.1016/j.newar.2017.09.002)
- Xue, Y. Q., Zheng, X. C., Li, Y., et al. 2019, Nature, 568, 198, doi: [10.1038/s41586-019-1079-5](https://doi.org/10.1038/s41586-019-1079-5)
- Yang, G., Brandt, W. N., Luo, B., et al. 2016, ApJ, 831, 145, doi: [10.3847/0004-637X/831/2/145](https://doi.org/10.3847/0004-637X/831/2/145)
- Yang, G., Boquien, M., Buat, V., et al. 2020, MNRAS, 491, 740, doi: [10.1093/mnras/stz3001](https://doi.org/10.1093/mnras/stz3001)
- Zubovas, K. 2019, MNRAS, 483, 1957, doi: [10.1093/mnras/sty3211](https://doi.org/10.1093/mnras/sty3211)